ACS OMEGA

http://pubs.acs.org/journal/acsodf

Article

Design of Experiments and Optimization of Laser-Induced Graphene

Richard Murray, Micheal Burke, Daniela Iacopino, and Aidan J. Quinn*

Cite This: *ACS Omega* 2021, 6, 16736−16743

Read Online

ACCESS | Metrics & More | Article Recommendations | Supporting Information

ABSTRACT: Realization of graphene-based sensors and electronic devices remains challenging, in part due to integration challenges with current fabrication and manufacturing processes. Thus, scalable methods for in situ fabrication of high-quality graphene-like materials are essential. Low-cost CO_2 laser engravers can be used for site-selective conversion of polyimide under ambient conditions to create 3-D, rotationally disordered, few-layer, porous, graphene-like electrodes. However, the influences of non-linear parameter terms and interactions between key parameters on the graphitization process present challenges for rapid, resource-efficient optimization. An iterative optimization strategy was developed to identify promising regions in parameter space for two key parameters, laser power and scan speed, with the goal of optimizing electrode performance while maximizing scan speed and hence fabrication throughput. The strategy employed iterations of Design of Experiments Response Surface (DoE-RS) methods combined with choices of readily measurable parameters to minimize measurement resources and time. The initial DoE-RS experiment set employed visual response parameters, while subsequent iterations used sheet resistance as the optimization parameter. The final model clearly demonstrates that laser graphitization through raster scanning is a highly non-linear process requiring polynomial terms in scan speed and laser power up to fifth order. Two regions of interest in parameter space were identified using this strategy: Region 1 represents the global minimum for sheet resistance for this laser (∼16 Ω/sq), found at a low scan speed (70 mm/s) and a low average power (2.1 W) . Region 2 is a local minimum for sheet resistance (36 Ω/sq), found at higher values for scan speed (340 mm/s) and average power (3.4 W), allowing ∼5-fold reduction in write time. Importantly, these minima do not correspond to constant ratios of average laser power to scan speed. This highlights the benefits of DoE-RS methods in rapid identification of optimum parameter combinations that would be difficult to discover using traditional one-factor-at-a-time optimization. Verification data from Raman spectroscopy showed sharp 2D peaks with mean full-width-at-half-maximum intensity values <80 cm^{-1} for both regions, consistent with high-quality 3D graphene-like carbon. Graphene-based electrodes fabricated using the parameters from the respective regions yielded similar performance when employed as capacitive humidity sensors with hygroscopic dielectric layers. Devices fabricated using Region 1 parameters (16 Ω/sq) yielded capacitance responses of 0.78 ± 0.04 pF at 0% relative humidity (RH), increasing to 31 ± 7 pF at 85.1% RH. Region 2 devices (36 Ω/sq) showed comparable responses (0.88 ± 0.04 pF at 0% RH, 28 ± 5 pF at 85.1% RH).

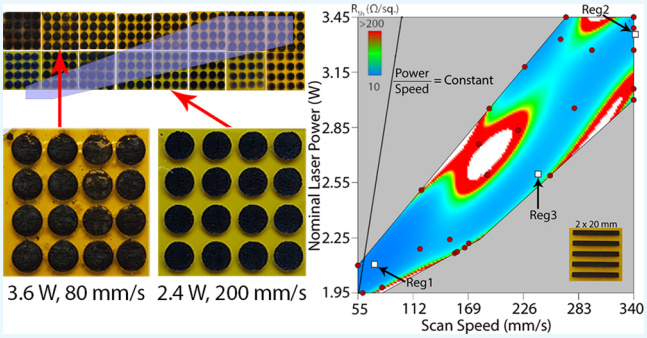

INTRODUCTION

Graphene and graphene-like materials, since their discovery, have been an exciting area of investigation for material science. High carrier mobility, thermal conductivity, tensile strength, zero band gap, and ballistic transport have been demonstrated for the most part in micron-scale pristine monolayer graphene, usually created by mechanical exfoliation.[1−7] This slow, non-scalable method hinders application development, such as graphene-based sensors.[8−10]

Several routes have been proposed to develop graphene-like materials with methods suited to scalable fabrication. Examples include chemical vapor-deposited graphene, reduced graphene oxide, and liquid-phase exfoliated graphene. Each approach can be assessed in terms of graphene quality and throughput. Transfer of chemical vapor deposition (CVD)-grown mono- or few-layer graphene from metal catalyst foil substrates (∼1−100 cm lateral dimensions) typically requires long processing times and the use of protective polymer handling layers. The residue from these layers presents challenges including unintentional heterogeneous doping and also tunnel barriers which can cause large contact resistance. Typical sheet resistance values usually exceed 500 Ω/sq for air-stable devices, consistent with the expected reduction in sheet resistance from pristine monolayer graphene (∼6 k Ω/sq measured in vacuum for mechanically

Received: January 18, 2021
Accepted: April 16, 2021
Published: June 23, 2021

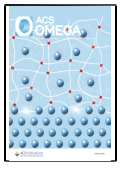

exfoliated monolayers) due to adsorbate doping from ambient water vapor or process residue.[11−13]

Liquid-based dispersions of graphene-derived nanomaterials such as reduced graphene oxide or liquid-phase exfoliated graphene offer ease of processing and compatibility with printing methods. However, the small crystallite size (35−600 nm) and the presence of process-induced basal plane and edge defects result in an increased sheet resistance (2 kΩ/sq) and variability.[14] Further, post-deposition curing (250−500 °C) is usually required, which can also present challenges for some applications.[15]

Although the production of graphitic materials through laser graphitization has been awarded patents as far back as 1972, little insight was achieved into the resulting material.[16,17] Tour and co-workers pioneered direct-write fabrication of porous three-dimensional (3D) laser-induced graphene (LIG) electrodes, beginning with laser graphitization of polyimide using CO_2 lasers.[18] The local high-temperature and high-pressure environment created by the laser photons breaks C−O, C═O, and C−N bonds of the polyimide, producing high-pressure gas pockets that drive the formation of micropores, nanopores, and other structural defects, resulting in a porous 3D structure that could not be achieved through annealing alone.[19−21]

Raman spectroscopy revealed well-resolved, narrow D, G, and 2D line shapes, consistent with the formation of graphene-like carbon with low disorder. Significant I_{2D}/I_G ratios and a distinct shoulder in the G line shape (corresponding to a D′ defect peak) are characteristic of high-quality graphene-like carbon. The symmetric 2D line shape contrasts with the asymmetric 2D peak reported for Bernal-stacked (ABAB) multilayer graphene or graphite[22,23] and suggests that laser-fabricated graphene is more likely to comprise few-layer graphene structures with rotational and/or vertical stacking disorder. This distinguishes LIG from pristine monolayer or few-layer graphene, which comprises planar single-crystal regions with lower defect densities.

Laser graphitization thus represents an exciting technology for direct integration of porous 3D graphene electrodes on polymer substrates. While the most promising feedstock material is polyimide, Tour and co-workers as well as other groups have demonstrated the formation of graphene-like carbon using a range of synthetic polymers and natural materials, including wood, food, textiles, charcoal, and anthracite coal.[24−26] To achieve these conversions, multiple-laser passes at reduced fluences, including use of defocused lasers to enhance laser-path overlap, are used to produce suitable quality LIG.[27] For each feedstock material, optimization of the laser graphitization process involves identification of a suitable set (or range) of process parameters, including (average) laser power and scan speed, that will yield direct-write formation of 3D porous, graphene-like carbon. Non-optimal laser parameters can lead to unwanted side effects from over- or under-exposure. Over-exposure effects include material ablation, redeposition, oxidation (ashing), or combinations of these. Under-exposure effects include melting and/or incomplete graphitization. This complex materials challenge mandates optimization strategies that are both rigorous and efficient.

This optimization challenge can be addressed using machine learning methods,[28−31] which require large data sets or statistically-driven methods, such as design of experiments (DoE).[32] Machine learning methods have gained increased popularity as computational resources have increased, removing their previous analysis bottleneck. They come in many different varieties, each depending on different algorithms for modeling supplied data. Data sets containing numerous potential factors that require both reduced dimensionality and modeling may benefit from principal component regression, while highly intricate systems may be more easily modeled by an ensemble method like random forests. More generic approaches could be used to facilitate more rapid model preparation, such as neural networks. For resource-constrained applications, the major drawback of machine learning approaches is the requirement for large data sets of training data to produce a model.[28−31]

Resource-efficient optimization mandates minimization of resources (including time) used to generate and analyze data. Machine learning methods reduce the analysis load but increase the required data set size and hence the resources required to produce those samples. DoE methods extract maximum information from a lean, statistically significant data set. DoE ensures that minimal samples are produced—reducing experimental cost—while ensuring that sufficient samples are tested to account for variability. The decreased number of samples required to be produced and tested comes at the cost of increased analysis.

The distinction between machine learning and DoE methods is clear: when large data sets are readily available, then machine learning should be preferred; if sample fabrication is resource-intensive, then DoE methods are favored. Highly complex systems can be simplified through iterative implementation of DoE methods. Each simplification step screens out insignificant factors and targets parameter ranges of interest. This stepwise process allows for dynamic decision making and scaled resource commitment not possible through less agile investigative tools. Similarly, DoE produces a documented search path with explicitly defined assumptions, not always generated with machine learning. Therefore, initial screening experiments, followed by informed, iterative optimization, require less resources than an equivalent mchine learning study.

Here, we report on an iterative DoE response surface (DoE-RS) strategy for identification of promising regions in the laser power versus scan speed parameter space for an entry-level CO_2 laser system, which would be within the budget of many research and teaching labs. Our goal is to optimize electrode performance while maximizing scan speed and hence fabrication throughput. DoE-RS optimization methods are well recognized as significantly more efficient than traditional one-factor-at-a-time methods. Further, DoE-RS approaches enable rigorous optimization even when there are non-linear interdependencies between input parameters.[33−35] DoE-RS approaches enable additional statistical efficiency by utilizing non-rectangular regions in parameter space to avoid non-viable regions with the added benefit of reduced experimental cost (resources and time).

Each iteration of the strategy focused on a readily measurable parameter to further minimize measurement resources and time. The initial DoE-RS iteration employed visual response parameters, while subsequent DoE-RS iterations optimized sheet resistance. We note that optimization strategies for graphene-based electronic or electrochemical sensing elements often include minimizing access resistance as a target in order to reduce *iR* potential drops that can diminish sensor performance and also energy efficiency.[36] Finally, we report on an iterative DoE screening approach to identify key

https://doi.org/10.1021/acsomega.1c00309
ACS Omega 2021, 6, 16736−16743

laser parameters and parameter interactions for a more sophisticated laser system, where the user has additional control over beam overlap within the raster pattern.

Since LIG electrodes and structures are produced by a dynamic patterning process which involves both temporal modulation of the laser output (through the duty cycle) and spatial patterning (through displacement of the laser head), optimization requires consideration of potential non-linear contributions of user-controlled parameters, including average laser power and scan speed, as well as potential interaction effects between these parameters.

RESULTS AND DISCUSSION

In the first report of LIG, Tour and co-workers reported a dependence of sheet resistance on laser power with a threshold of 2.4 W at ∼90 mm/s using a Universal Laser System X-660 CO_2 laser system and achieved minimum sheet resistances (∼15 Ω/sq) at 5.4 W, ∼90 mm/s through one-factor-at-a-time (OFAT) optimization. These authors also noted that a linear dependence of the threshold power for graphitization on the scan speed.[18] This observed interaction of factors suggests that both laser power and scan speed should be considered simultaneously, since underlying mechanisms may not be observable through OFAT methods.

DOE methods were implemented in this work to illustrate their ability to determine relationships between factors in materials synthesis and for rapid, iterative resource-efficient material optimization, even with an entry-level hobbyist laser system. Initially, visual inspection was used to identify laser power and scan speed parameters which yielded viable or unviable samples. Figure 1a shows an example of an unviable sample with cracked, inhomogeneous material, while a viable sample with homogeneous, deep black material can be seen in Figure 1b. This visual inspection was further refined through the response surface design of experiment (DOE-RS) process based on qualitatively measured visual responses (fibrosity, residue, and damage), as seen in Figure S2. The model indicated that lower average laser powers (2.4−3.9 W for our hobbyist laser system) and higher scan speeds (280−440 mm/s) yielded fewer defects. A subsequent sheet resistance-based DOE-RS (Figure S3) showed a region of low sheet resistance at low laser powers (2.4−5.4 W) and moderate scan speeds (200−440 mm/s) that tapers as laser power and scan speed increase. This model suggested that the global sheet resistance minimum for this laser system could be found at even lower values of laser power and scan speed, which informed the parameter ranges used in the final iteration of our DOE-RS, shown in Figure 1d.

The response surface model is based on a polynomial fit built from statistically significant terms (Table S4). Up to fifth-order terms in scan speed and fourth-order terms of laser power were seen to be significant. Lower-order terms and cross-terms were also included. Table S5 shows the significance of each term. The p-value (<0.0001) for the final model confirms the statistical significance of the terms. Further, the residual lack of fit was insignificant (a p-value of 0.44), suggesting confidence in the model chosen and its predictions. Response surface zones colored in white could not be fit with the model, likely indicating non-viable conditions for graphitization or a low-quality material. Three specific "regions of interest" are labeled on the response surface: the predicted global minimum sheet resistance (region 1), a local minimum at a high scan speed (region 2), and an interim point (region 3).

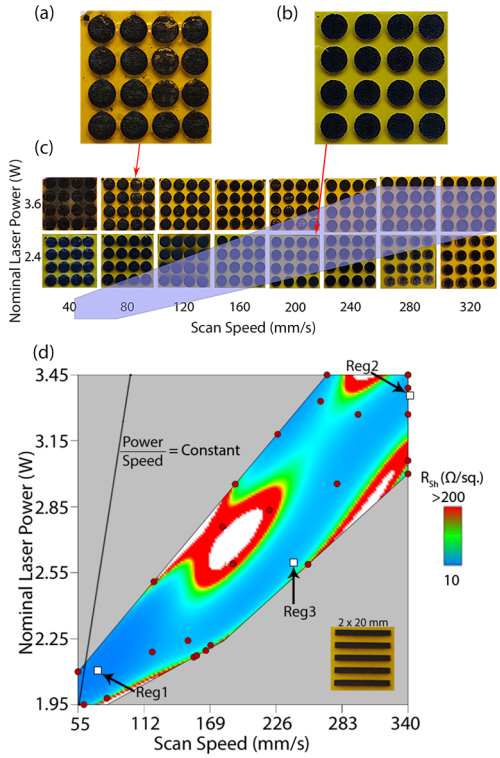

Figure 1. (a) Photo showing test structures (4 mm diameter discs) fabricated using "unviable" laser parameters (80 mm/s raster scan speed, 3.6 W average power) which yield laser-induced defects such as cracks and delamination. (b) Photo of "viable" test structures showing uniform, black material (200 mm/s scan speed, 2.4 W average power). (c) Subset of the overall grid layout of test structure photos organized by scan speed and laser power (full layout in Figure S1). The shaded region indicates the final response surface parameter domain. (d) DoE-RS model output for sheet resistance vs laser power and raster scan speed factors. Arrows indicate the regions of interest for further characterization: global minimum for sheet resistance (Reg. 1), minimum sheet resistance at a high scan speed (Reg. 2), and a local minimum resistance at an intermediate scan speed (Reg. 3). Inset: Photo of an array of 20 mm × 2 mm test structures used for sheet resistance measurements.

Table 1 shows the predicted sheet resistances for the three regions of interest and the corresponding experimental sheet resistance values. Region 1 and region 2 samples yield predicted and measured sheet resistance values that agree within a factor 2. Importantly, the model allows identification of region 2, where low sheet resistance can still be achieved while increasing scan speed by a factor ∼5. The measured sheet resistance for region 3 is over an order of magnitude higher than the predicted model value. This discrepancy could

Table 1. Predicted and Actual Sheet Resistance Values from Linear $I-V$ data (−3 to 3 V) for Samples Fabricated Using Laser Parameters for Regions 1−3

parameter space region	laser power (W)	scan speed (mm/s)	predicted sheet res. (Ω/sq)	mean sheet res. (Ω/sq.)
1	2.1	70	10	15.7 ± 0.7
2	3.4	340	26	36 ± 1
3	2.6	240	37	410 ± 180

https://doi.org/10.1021/acsomega.1c00309
ACS Omega 2021, 6, 16736−16743

be due to the high curvature of the model in this zone of the parameter space, where a small fluctuation of the laser parameters could result in a large change in sheet resistance.

Figure 2 shows the morphology associated with the three regions of interest. A hierarchical pore structure with micron-

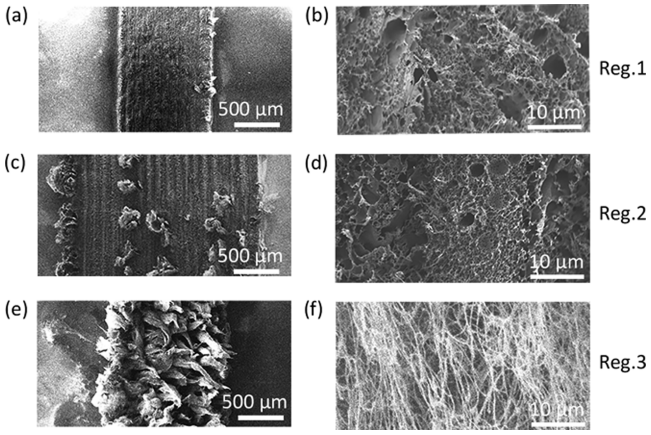

Figure 2. SEM data at low and higher magnifications, respectively, for samples fabricated using laser power and scan speed parameters from region 1 (a,b), region 2 (c,d), and region 3 (e,f).

scale and sub-micron pore diameters can be observed in samples fabricated using parameters for Region 1 (Figure 2a,b) and for Region 2 (Figure 2c,d). In addition, the Region 2 sample also shows a higher density of 3D extrusions. The morphology of the Region 3 sample differs markedly from the samples for Regions 1 and 2. There is no longer a clear porosity; instead, the surface comprises sub-mm 3D extrusions (Figure 2e) comprising networks of micron-scale fibers (Figure 2f).

Cross-sectional scanning electron microscopy (SEM) micrographs obtained for Region 1 samples show an approximate LIG thickness of 50 μm (Figure S6). This agrees with thickness values observed by Duy et al., who noted LIG thickness self-limits to <50 μm. The maximum conversion depth is caused by the conversion beginning at the surface, attenuating the conversion of the sub-surface material.[27] As such, it is assumed that both Region 1 and Region 2 materials are of approximately the same thickness. However, Figure 2c shows that the Region 2 material contains some vertical extrusions. These structures could reduce the available lateral charge-transfer pathways and are likely partly responsible for the increased sheet resistance of Region 2 materials. Assuming an LIG thickness of 50 μm, the corresponding resistivity for Region 1 material is 7.8×10^{-4} Ω m, reflecting the expected disorder on the device length scale (2 cm).

Stamatin et al. have reported on the morphology of laser-graphitized polyimide in terms of a similar metric[38]

$$\text{dynamic fluence} = \frac{\text{laser power}}{\text{scan speed} \times \text{beam diameter}}$$

They calculated dynamic fluence values ranging from 0.3 to 4.8 J/mm^2. For this work, initial rough estimates of the dynamic fluence can be made using the raster pitch as the beam diameter (~90 μm for the region 1 material, see Figure 2a). In this way, the initial estimates of dynamic fluence are 0.33 J/mm^2 (region 1), 0.11 J/mm^2 (region 2), 0.12 J/mm^2 (region 3).

However, dynamic fluence values consider only single laser passes without accounting for beam overlap between neighboring lines in the raster pattern, ~85 μm (Figure S8). Tour et al., as previously noted, demonstrated that multi-pass lasing can produce LIG even at reduced laser intensities upon subsequent re-exposure.[27] Consequentially, a reduction of dynamic fluence values, relative to those reported by Stamatin et al., is expected due to the beam overlap from rastering.

Moreover, the fact that regions 1 and 2 do not lie on a line representing a constant ratio of (average) laser power to scan speed (Figure 1d) highlights the non-linearity of the parameter dependencies for laser graphitization, which would not be uncovered by traditional one-factor (OFAT) optimization. This is especially significant as the beam profile can vary with laser power, further convolving any laser power dependence and any overlap dependence. This increases the complexity of investigating the parameter space and highlights the potential of DoE-RS methods to facilitate optimization, especially for resource-constrained processes. It allowed us to achieve similar sheet resistance values but with an almost 5-fold increase in scan speed and hence throughput.

Figure 3 shows representative Raman spectra from maps taken over samples fabricated with Region 1, 2, and 3 parameters. Table S6 shows the corresponding Lorentzian fit results. For the Region 3 material, the D′ and D + D″ peaks

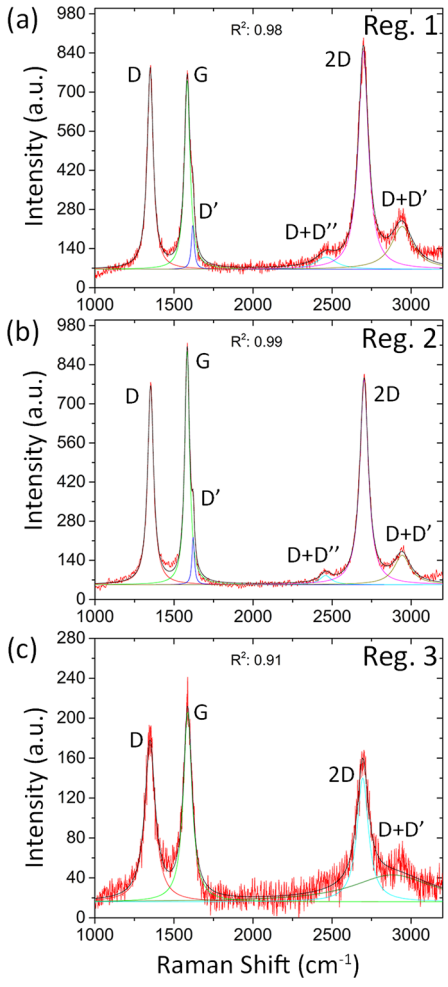

Figure 3. Representative Raman spectra of the (a) region 1, (b) region 2, and (c) region 3 LIG materials.

https://doi.org/10.1021/acsomega.1c00309
ACS Omega 2021, 6, 16736−16743

could not be resolved, the D and G peaks are distinctly broader, and the I_D/I_G and I_{2D}/I_G areal ratios are smaller than those for Region 1 and Region 2 samples. This suggests increased disorder and defect density in the Region 3 material, consistent with the morphology (Figure 2f). In early Raman studies of graphite, D′ peak signatures were observed in high-quality polycrystalline graphite and also by creating defects in natural graphite single crystals. D′ shoulders similar to the data shown in Figure 3a, b were observed in polycrystalline graphite with domain sizes (or scattering coherence lengths) ≈7−12 nm.[39,40] The highly intense G peak of the region 1 and region 2 materials, their resolvable D′ peak, and sharp D and 2D peaks are suggestive of a high-quality graphene-like material with defects present.

Figure 4a,b shows fit data [Raman full width at half-maximum (fwhm), peak area as a ratio of the area under the G peak] from 14 random locations for samples from each region, plotted versus peak position. Spectra from samples fabricated with Region 1 or Region 2 parameters show similar clustering of fit results for the first-order peaks (D, G, and D′), while spectra from samples with Region 3 parameters present a larger distribution of values. This clustering treatment demonstrates that Regions 1 and 2 are similar despite the Region 2 material being produced at 5 times the scan speed of the Region1 material. The larger fwhm (D) values for Region 3 indicate significant disorder, in agreement with the observed sample morphology (Figure 2e,f).

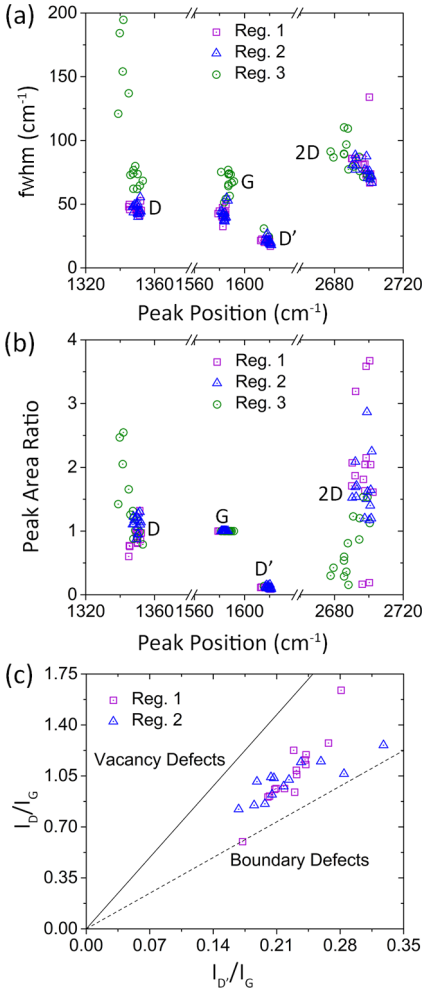

Figure 4. a) fwhm of Raman peaks vs peak position; (b) peak area ratios relative to the G peak vs peak position. (c) I_D/I_G vs $I_{D'}/I_G$ with lines indicating values expected for boundary defects (dashed line) and vacancy defects (solid line).

Detailed Raman spectroscopy studies by Eckmann et al. on exfoliated monolayer graphene with deliberately introduced defects and natural graphite established empirical relationships between the ratios of the D to D′ peaks and the nature of the defects:[41] $I(D)/I(D') \sim 13$ for sp3 defects, $I(D)/I(D') \sim 7$ for vacancy defects, and $I(D)/I(D') \sim 3.5$ for boundary defects in natural graphite. Data measured for region 1 and region 2 samples showed $I(D)/I(D')$ values between 3.5 and 7 (Figure 4c), again consistent with low disorder. The presence of such defects is expected give the LIG formation process: Stone−Wales defects enable the 3D curvature, and every pore acts as a series of edge defects. As such, the presence of boundary and vacancy defects is expected and intrinsic to the material. However, it may provide scope for further tuning of laser parameters toward boundary/vacancy-dominated defects if it proves to be a desirable parameter.

As LIG is formed in situ with the mechanical support of its substrate, it has attracted great interest as a gas sensing platform. Sensing devices based on electrical conductivity or thermal conductivity changes in the presence of volatile organic compounds have been reported.[42,43] The presence of humidity is a major challenge for volatile organic compound sensing as water molecules can block sites or lead to spurious responses. Therefore, due to their similarity in observed properties (sheet resistance, morphology, and Raman data), both Region 1 and Region 2 laser parameters were used to produce proof-of-concept LIG humidity sensors. Interdigitated electrode patterns were laser-fabricated (Figure 5, inset) and functionalized with polyvinyl alcohol (PVA) as a hygroscopic dielectric material to produce capacitive humidity sensors (six devices for each region). Similar exponential capacitive responses were observed for both Region 1 and Region 2 materials with over an order of magnitude increase with increasing relative humidity (RH). Region 1 parameter devices yielded capacitance responses of 0.78 ± 0.04 pF at 0% RH, increasing to 31 ± 7 pF at 85.1% RH. Region 2 devices showed comparable responses (0.88 ± 0.04 pF at 0% RH, 28 ± 5 pF at 85.1% RH).

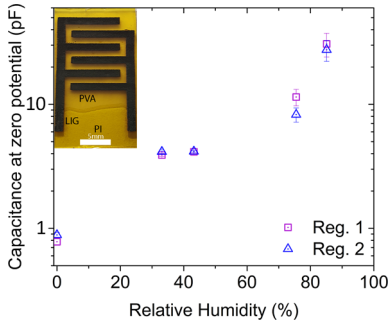

Figure 5. Exponential dependence of capacitance at zero potential (2 kHz) on RH for PVA-functionalized LIG capacitance humidity sensors produced under Region 1 and 2 conditions. Inset: photo of the interdigitated PVA-LIG capacitive humidity sensor.

Device time responses and reversibility were also measured by switching between different humidity conditions (33.3% RH to 85.5% RH and vice versa, Figure S7). The time taken to

https://doi.org/10.1021/acsomega.1c00309
ACS Omega 2021, 6, 16736−16743

reach 90% of the maximum capacitance (t_{Ads} = 37.5 min) was significantly longer than the time taken to return to 90% of the final capacitance (t_{Des} = 2.0 min), suggesting an adsorption barrier energy. This could be addressed in future work through use of thinner films of hygroscopic dielectrics or integration of an external heater to reduce response and recovery times, respectively.[44] The similarity of the resulting humidity sensors highlights the ability of DoE-RS methods to determine potentially useful regions of interest in complex material systems.

Finally, the demonstrated ability of DoE-RS methods to rapidly investigate interactions between factors provides a broad scope for future work in specific device geometry optimizations. Additional factors can be considered, especially the interaction of raster beam overlap with laser power and scan speed. Many-factor interactions are demonstrated in Section S8 with proof-of-concept iterative DOE-RS methods using a higher fidelity laser system (Universal Laser Systems PLS 4.75 30 W CO_2 10.6 μm). This laser system allows user control of the laser scan speed and the average laser power (achieved by varying the duty cycle of the electrical modulation waveform). The system also allows user control of the line−line overlap during rastering, the focus height above the sample, the gas flow through the nose cone above the focal plane (nitrogen or air), and the electrically gated modulation rate of the laser along the main raster direction (pulses per inch, PPI). Screening experiments indicated that the laser modulation rate in the range studied (500−1000 PPI) and gas flow were not significant factors for controlling sheet resistance. A subsequent optimization round highlighted the significance of line−line overlap both as a main factor and in interactions. As discussed earlier, the multi-pass lasing methods developed by Tour et al.[25] revealed the importance of device history effects, including raster beam overlap and laser defocusing. Significant beam overlap between raster lines during patterning and/or multiple-pass lasing can result in LIG formation at reduced dynamic fluence values relative to structures produced by single laser passes, as reported by Stamatin et al. The complex, non-linear contributions from key parameters (laser power, scan speed, and beam overlap) highlight the benefits and importance of DoE-RS optimization methods. Where application-specific device geometries are known, further optimization may be possible by considering the raster/vector direction, the beam profile, and time- or history-dependent effects such as thermal relaxation of the substrate between laser passes.

CONCLUSIONS

This work reported the successful use of design of experiment methods in the determination of optima and factor interactions in complex, novel material systems. Iterative DoE processes were demonstrated, realizing both a global minimum for sheet resistance and a local minimum at high scan speed. Despite uncertainty in the LIG formation mechanism, it was possible to determine these two non-intuitively connected regions possessing similar material properties despite distinct formation conditions. Consequentially, all-polymer humidity sensors were successfully produced with the LIG materials functionalized with PVA, displaying equivalent sensitivities. This demonstration of 5× higher fabrication throughput highlights the potential of design of experiment methods as an investigative tool.

The employment of design of experiment methods in this work demonstrates not only its efficiency as an optimization strategy but also its use as a rigorous, resource-efficient investigation tool. The use of DOE methods allows for appropriate investment of resources at different phases of the process, retaining higher-expense experiments, both in analysis time and operational cost, for smaller sampling regions and verification processes. This helps to maximize throughput and ensure efficient experimental design. Consequentially, regions of interest can be determined rapidly, and time can be spent focusing on high-quality, cutting edge work instead of screening steps. For instance, the implementation of in-depth Raman surveys would be impractical on large parameter spaces, while for verification processes, their added rigor can be appropriately utilized. This work highlights the importance of such optimization strategies for "all-carbon" sensor elements, where use of metals or other critical raw materials is not favored in order to minimize the environmental footprint and economic costs.

METHODS

Sample Preparation and Visual Inspection. A low-cost (~$500) CO_2 laser engraver [10.6 μm wavelength, 0−30 W power (oscillating mirror modulation), HQ-3020B, GuangZhou Amonstar Trade Co., Ltd.] was rastered under ambient conditions to convert adhesive-backed polyimide film (Radionics, HB830-19, thickness: 70 μm), supported by an acrylic substrate, into a graphitic material. A parameter space of 6 values of average laser powerin the range of 2.4−8.4 W and 11 scan speed values in the range of 40−440 mm/s was investigated by producing a series of samples on polyimide for a subset of 60 combinations of laser power and scan speed, as shown in Figure S1. Each sample (16 discs, each ~4 mm diameter) was visually inspected to determine the bounds of the uniform, black, non-damaged material—a useful visual indicator for LIG.

Iterative DoE Methodology. The region of interest derived from the visual inspection was used to define a screening DoE-RS (Design Expert 11) based on visually graded responses (fibrosity, redeposited residue, and damage) as assessed on a scale of 1−10 (Figure S2). Informed by this visual screening DoE-RS, a further 18-point screening DoE-RS using a sheet resistance response factor was constructed, as shown in Figure S3. Transfer line measurement tracks were produced with lengths of 1.5−6 mm and widths of 0.5−1.8 mm. The resistances were recorded using a multimeter (Fluke 179), and the corresponding sheet resistances were extracted. The average sheet resistance from five transfer line measurement structures was used for the DoE-RS. Predicted optima at low−moderate values of laser power and scan speed were investigated by a subsequent 30-point DoE-RS using a sheet resistance response. Each sample for this final DoE-RS comprised five replicates of 20 mm × 2 mm bar structures (10:1 aspect ratio). The use of long, high-aspect-ratio bar structures minimizes the influence of contact resistance by ensuring that it is a small proportion of the total recorded resistance, while retaining high throughput of measurements. The inclusion of replicates was to account for any variability in the contact resistance. A DoE-RS model was constructed using an inverse transformation and fifth-order polynomial terms, as described in Section S2 in the Supporting Information.

Three regions of interest were identified from the final response surface experiments (Region 1, Region 2, and Region

https://doi.org/10.1021/acsomega.1c00309
ACS Omega 2021, 6, 16736−16743

3). Five replicates of the 20 mm × 2 mm structures were produced using the DoE-RS model parameters for each region. Current−voltage sweeps (−3 to +3 V) were obtained (Desert cryogenic probe station with an Agilent E4980A parameter analyzer) to verify the multimeter measurements. The associated sheet resistance values were calculated.

Raman Spectroscopy Measurements and Analysis. Samples produced under the Region 1, Region 2, and Region 3 conditions were characterized by Raman spectroscopy mapping (Renishaw inVia, 514.5 nm Ar laser, 20× and 50× objectives). To account for the 3D structure and sample inhomogeneity, numerous scans were taken as part of a Raman map of each location. Mapping was conducted at 20× and 50× magnifications at three spatially distinct locations across two separate samples. A total of 228 scans were obtained for Region 1 samples, 230 for Region 2 samples, and 219 for Region 3 samples. All scans for Region 1 and Region 2 samples displayed graphitic behavior. For Region 3 samples, ∼70% of the spectra showed graphitic peaks (158 of 219); the remaining 61 displayed only the background associated with scattering from a highly 3D sample.

Of the scans that displayed graphitic behavior, 14 spectra were randomly selected for detailed peak fitting. Spectra from Region 1 and Region 2 samples were fit with six Lorentzian peaks—three first-order Raman peaks (D, G, and D′) and three second-order peaks (D + D″, 2D, and D + D′). Spectra from Region 3 samples were fit with four peaks since the D′ and D + D″ peaks could not be resolved. The mm-scale and microscale morphologies of the samples were characterized by SEM (JSM-6700F JEOL UK Ltd.).

Proof-of-Concept Humidity Sensing. Interdigitated electrodes were fabricated using the predicted DoE-RS parameters for two minima: the global minimum sheet resistance (Region 1) and minimum sheet resistance at a high scan speed (Region 2). PVA was doctor-bladed onto the electrodes to create a hygroscopic dielectric layer for proof-of-concept capacitance-based humidity sensors. The capacitance sensors (six individual devices for each region of interest) were equilibrated for 6 h above saturated salt solutions, producing standard humidity environments according to the E104-02 standard, that is, vacuum: 0% RH; MgCl: 33.1% RH; K_2CO_3: 43.2% RH; NaCl: 75.5% RH; KCl 85.1% RH.[37] The capacitance response was measured using an AC potential sweep (Agilent E53708B LCR Meter, 2 kHz).

■ ASSOCIATED CONTENT

Supporting Information

The Supporting Information is available free of charge at https://pubs.acs.org/doi/10.1021/acsomega.1c00309.

DoE: introduction and overview; iterative DoE optimization; Raman fit results; electrical characterization; cross-section SEM; proof-of-concept humidity sensing: time constants; beam overlap estimates (HQ-3020B laser); and multi-parameter DoE screening (PLS laser) (PDF)

■ AUTHOR INFORMATION

Corresponding Author

Aidan J. Quinn − *Tyndall National Institute, University College Cork, Cork T12R5CP, Ireland;* orcid.org/0000-0003-4021-9990; Email: aidan.quinn@tyndall.ie

Authors

Richard Murray − *Tyndall National Institute, University College Cork, Cork T12R5CP, Ireland;* orcid.org/0000-0003-0676-5111

Micheal Burke − *Tyndall National Institute, University College Cork, Cork T12R5CP, Ireland;* orcid.org/0000-0003-1831-8829

Daniela Iacopino − *Tyndall National Institute, University College Cork, Cork T12R5CP, Ireland;* orcid.org/0000-0003-2301-9401

Complete contact information is available at: https://pubs.acs.org/10.1021/acsomega.1c00309

Notes

The authors declare no competing financial interest.

■ ACKNOWLEDGMENTS

This publication has emanated from research conducted with the financial support of Science Foundation Ireland (SFI) under grant numbers SFI 16/RC/3918 (CONFIRM) and 13/RC/2077 (CONNECT), co-funded by the European Regional Development Fund.

■ REFERENCES

(1) Bolotin, K. I.; Sikes, K. J.; Jiang, Z.; Klima, M.; Fudenberg, G.; Hone, J.; Kim, P.; Stormer, H. L. Ultrahigh Electron Mobility in Suspended Graphene. *Solid State Commun.* **2008**, *146*, 351−355.

(2) Chen, G.; Liu, Y.; Liu, F.; Zhang, X. Fabrication of Three-Dimensional Graphene Foam with High Electrical Conductivity and Large Adsorption Capability. *Appl. Surf. Sci.* **2014**, *311*, 808−815.

(3) Balandin, A. A.; Ghosh, S.; Bao, W.; Calizo, I.; Teweldebrhan, D.; Miao, F.; Lau, C. N. Superior Thermal Conductivity of Single-Layer Graphene. *Nano Lett.* **2008**, *8*, 902−907.

(4) Lee, C.; Wei, X.; Kysar, J. W.; Hone, J. Measurement of the Elastic Properties and Intrinsic Strength of Monolayer Graphene. *Science* **2008**, *321*, 385−388.

(5) Meric, I.; Han, M. Y.; Young, A. F.; Ozyilmaz, B.; Kim, P.; Shepard, K. L. Current Saturation in Zero-Bandgap, Top-Gated Graphene Field-Effect Transistors. *Nat. Nanotechnol.* **2008**, *3*, 654−659.

(6) Xia, J.; Chen, F.; Li, J.; Tao, N. Measurement of the Quantum Capacitance of Graphene. *Nat. Nanotechnol.* **2009**, *4*, 505−509.

(7) Du, X.; Skachko, I.; Barker, A.; Andrei, E. Y. Approaching Ballistic Transport in Suspended Graphene. *Nat. Nanotechnol.* **2008**, *3*, 491−495.

(8) Murali, R.; Brenner, K.; Yang, Y.; Beck, T.; Meindl, J. D. Resistivity of Graphene Nanoribbon Interconnects. *IEEE Electron Device Lett.* **2009**, *30*, 611−613.

(9) Mohan, V. B.; Lau, K.-t.; Hui, D.; Bhattacharyya, D. Graphene-Based Materials and Their Composites: A Review on Production, Applications and Product Limitations. *Composites, Part B* **2018**, *142*, 200−220.

(10) Schedin, F.; Geim, A. K.; Morozov, S. V.; Hill, E. W.; Blake, P.; Katsnelson, M. I.; Novoselov, K. S. Detection of Individual Gas Molecules Adsorbed on Graphene. *Nature Mat.* **2007**, *6*, 652−655.

(11) Gahoi, A.; Wagner, S.; Bablich, A.; Kataria, S.; Passi, V.; Lemme, M. C. Contact Resistance Study of Various Metal Electrodes with CVD Graphene. *Solid State Electron.* **2016**, *125*, 234−239.

(12) Suk, J. W.; Kitt, A.; Magnuson, C. W.; Hao, Y.; Ahmed, S.; An, J.; Swan, A. K.; Goldberg, B. B.; Ruoff, R. S. Transfer of CVD-Grown Monolayer Graphene onto Arbitrary Substrates. *ACS Nano* **2011**, *5*, 6916−6924.

(13) Novoselov, K. S.; Morozov, S. V.; Mohinddin, T. M. G.; Ponomarenko, L. A.; Elias, D. C.; Yang, R.; Barbolina, I. I.; Blake, P.; Booth, T. J.; Jiang, D.; Giesbers, J.; Hill, E. W.; Geim, A. K. Electronic Properties of Graphene. *Phys. Status Solidi* **2007**, *244*, 4106−4111.

(14) Finn, D. J.; Lotya, M.; Cunningham, G.; Smith, R. J.; McCloskey, D.; Donegan, J. F.; Coleman, J. N. Inkjet Deposition of Liquid-Exfoliated Graphene and MoS2 Nanosheets for Printed Device Applications. *J. Mater. Chem. C* **2014**, *2*, 925−932.
(15) Niu, L.; Coleman, J. N.; Zhang, H.; Shin, H.; Chhowalla, M.; Zheng, Z. Production of Two-Dimensional Nanomaterials via Liquid-Based Direct Exfoliation. *Small* **2016**, *12*, 272−293.
(16) Epstein, A. Electrically Insulating Polymer Matrix with Conductive Path Formed in STU. U.S. Patent 4,841,099 A, 1989.
(17) Binning, R. C. Binning. Method of Graphitizing Fibers by Laser. U.S. Patent 3,699,210 A, 1972.
(18) Lin, J.; Peng, Z.; Liu, Y.; Ruiz-Zepeda, F.; Ye, R.; Samuel, E. L. G.; Yacaman, M. J.; Yakobson, B. I.; Tour, J. M. Laser-Induced Porous Graphene Films from Commercial Polymers. *Nat. Commun.* **2014**, *5*, 5714.
(19) Dreyfus, R. W. CN Temperatures above Laser Ablated Polyimide. *Appl. Phys. A: Solids Surf.* **1992**, *55*, 335−339.
(20) Ye, R.; James, D. K.; Tour, J. M. Laser-Induced Graphene: From Discovery to Translation. *Adv. Mater.* **2019**, *31*, 1803621.
(21) Dong, Y.; Rismiller, S. C.; Lin, J. Molecular Dynamic Simulation of Layered Graphene Clusters Formation from Polyimides under Extreme Conditions. *Carbon* **2016**, *104*, 47−55.
(22) Pimenta, M. A.; Dresselhaus, G.; Dresselhaus, M. S.; Cançado, L. G.; Jorio, A.; Saito, R. Studying Disorder in Graphite-Based Systems by Raman Spectroscopy. *Physical Chemistry Chemical Physics*; The Royal Society of Chemistry, 2007, pp 1276−1290.
(23) Lenski, D. R.; Fuhrer, M. S. Raman and Optical Characterization of Multilayer Turbostratic Graphene Grown via Chemical Vapor Deposition. *J. Appl. Phys.* **2011**, *110*, 013720.
(24) Ye, R.; Chyan, Y.; Zhang, J.; Li, Y.; Han, X.; Kittrell, C.; Tour, J. M. Laser-Induced Graphene Formation on Wood. *Adv. Mater.* **2017**, *29*, 1702211.
(25) Chyan, Y.; Ye, R.; Li, Y.; Singh, S. P.; Arnusch, C. J.; Tour, J. M. Laser-Induced Graphene by Multiple Lasing: Toward Electronics on Cloth, Paper, and Food. *ACS Nano* **2018**, *12*, 2176−2183.
(26) Ye, R.; James, D. K.; Tour, J. M. Laser-Induced Graphene. *Acc. Chem. Res.* **2018**, *51*, 1609−1620.
(27) Duy, L. X.; Peng, Z.; Li, Y.; Zhang, J.; Ji, Y.; Tour, J. M. Laser-Induced Graphene Fibers. *Carbon* **2018**, *126*, 472−479.
(28) Mannodi-Kanakkithodi, A.; Pilania, G.; Ramprasad, R. Critical Assessment of Regression-Based Machine Learning Methods for Polymer Dielectrics. *Comput. Mater. Sci.* **2016**, *125*, 123−135.
(29) Beleites, C.; Neugebauer, U.; Bocklitz, T.; Krafft, C.; Popp, J. Sample Size Planning for Classification Models. *Anal. Chim. Acta* **2013**, *760*, 25−33.
(30) Mundfrom, D. J.; Shaw, D. G.; Ke, T. L. Minimum Sample Size Recommendations for Conducting Factor Analyses. *Int. J. Test.* **2005**, *5*, 159−168.
(31) Hestness, J.; Narang, S.; Ardalani, N.; Diamos, G.; Jun, H.; Kianinejad, H.; Patwary, M. M. A.; Yang, Y.; Zhou, Y. Deep Learning Scaling Is Predictable, Empirically. **2017**, arXiv:1712.00409.
(32) Burke, M.; Blake, A.; Povey, I. M.; Schmidt, M.; Petkov, N.; Carolan, P.; Quinn, A. J. Low Sheet Resistance Titanium Nitride Films by Low-Temperature Plasma-Enhanced Atomic Layer Deposition Using Design of Experiments Methodology. *J. Vac. Sci. Technol., A* **2014**, *32*, 031506.
(33) Denmark, S. E.; Butler, C. R. Vinylation of Aromatic Halides Using Inexpensive Organosilicon Reagents. Illustration of Design of Experiment Protocols. *J. Am. Chem. Soc.* **2008**, *130*, 3690−3704.
(34) Anderson, M. J. *Know the SCOR for Multifactor Strategy of Experimentation: Screening, Characterization, Optimization and Ruggedness Testing*; Stat-Ease, Inc., 2014.
(35) Felice, C.; Qu, D. Optimization of the Synthesis of Nafion-Montmorillonite Nanocomposite Membranes for Fuel Cell Applications through Statistical Design-of-Experiment. *Ind. Eng. Chem. Res.* **2011**, *50*, 721−727.
(36) Vaughan, E.; Larrigy, C.; Burke, M.; Sygellou, L.; Quinn, A. J.; Galiotis, C.; Iacopino, D. Visible Laser Scribing Fabrication of Porous Graphitic Carbon Electrodes: Morphologies, Electrochemical Properties, and Applications as Disposable Sensor Platforms. *ACS Appl. Electron. Mater.* **2020**, *2*, 3279−3288.
(37) ASTM Standard E104-02. Astm E104. *Standard Practice for Maintaining Constant Relative Humidity by Means of Aqueous Solutions*; ASTM International, 2012, 02 (Reapproved 2012); pp 1−5.
(38) Tiliakos, A.; Ceaus, C.; Iordache, S. M.; Vasile, E.; Stamatin, I. Morphic Transitions of Nanocarbons via Laser Pyrolysis of Polyimide Films. *J. Anal. Appl. Pyrolysis* **2016**, *121*, 275−286.
(39) Nemanich, R. J.; Solin, S. A. First- and Second-Order Raman Scattering from Finite-Size Crystals of Graphite. *Phys. Rev. B* **1979**, *20*, 392−401.
(40) Lespade, P.; Al-Jishi, R.; Dresselhaus, M. S. Model for Raman Scattering from Incompletely Graphitized Carbons. *Carbon* **1982**, *20*, 427−431.
(41) Eckmann, A.; Felten, A.; Mishchenko, A.; Britnell, L.; Krupke, R.; Novoselov, K. S.; Casiraghi, C. Probing the Nature of Defects in Graphene by Raman Spectroscopy. *Nano Lett.* **2012**, *12*, 3925−3930.
(42) Stanford, M. G.; Zhang, C.; Fowlkes, J. D.; Hoffman, A.; Ivanov, I. N.; Rack, P. D.; Tour, J. M. High-Resolution Laser-Induced Graphene. Flexible Electronics beyond the Visible Limit. *ACS Appl. Mater. Interfaces* **2020**, *12*, 10902−10907.
(43) Stanford, M. G.; Yang, K.; Chyan, Y.; Kittrell, C.; Tour, J. M. Laser-Induced Graphene for Flexible and Embeddable Gas Sensors. *ACS Nano* **2019**, *13*, 3474−3482.
(44) Boudaden, J.; Steinmaßl, M.; Endres, H. E.; Drost, A.; Eisele, I.; Kutter, C.; Müller-Buschbaum, P. Polyimide-Based Capacitive Humidity Sensor. *Sensors* **2018**, *18*, 1516.

https://doi.org/10.1021/acsomega.1c00309
ACS Omega 2021, 6, 16736−16743